catalysts

MDPI

Article

Hydrothermal and Co-Precipitated Synthesis of Chalcopyrite for Fenton-like Degradation toward Rhodamine B

Po-Yu Wen [1], Ting-Yu Lai [1], Tsunghsueh Wu [2,*] and Yang-Wei Lin [1,*]

[1] Department of Chemistry, National Changhua University of Education, 1 Jin-De Road, Changhua City 50007, Taiwan; bba02123@gmail.com (P.-Y.W.); superhuman860731@gmail.com (T.-Y.L.)
[2] Department of Chemistry, University of Wisconsin-Platteville, 1 University Plaza, Platteville, WI 53818-3099, USA
* Correspondence: wut@uwplatt.edu (T.W.); linywjerry@cc.ncue.edu.tw (Y.-W.L.); Tel.: +1-608-342-6018 (T.W.); +886-4-7232105-3553 (Y.-W.L.)

Abstract: In this study, Chalcopyrite ($CuFeS_2$) was prepared by a hydrothermal and co-precipitation method, being represented as H-$CuFeS_2$ and C-$CuFeS_2$, respectively. The prepared $CuFeS_2$ samples were characterized by scanning electron microscope (SEM), transmission electron microscope (TEM), energy dispersive X-ray spectroscopy mapping (EDS-mapping), powder X-ray diffractometer (XRD), X-ray photoelectron spectrometry (XPS), and Raman microscope. Rhodamine B (RhB, 20 ppm) was used as the target pollutant to evaluate the degradation performance by the prepared $CuFeS_2$ samples. The H-$CuFeS_2$ samples (20 mg) in the presence of $Na_2S_2O_8$ (4 mM) exhibited excellent degradation efficiency (98.8% within 10 min). Through free radical trapping experiment, the major active species were $\bullet SO_4^-$ radicals and •OH radicals involved the RhB degradation. Furthermore, $\bullet SO_4^-$ radicals produced from the prepared samples were evaluated by iodometric titration. In addition, one possible degradation mechanism was proposed. Finally, the prepared H-$CuFeS_2$ samples were used to degrade different dyestuff (rhodamine 6G, methylene blue, and methyl orange) and organic pollutant (bisphenol A) in the different environmental water samples (pond water and seawater) with 10.1% mineral efficiency improvement comparing to traditional Fenton reaction.

Keywords: hydrothermal preparation; co-precipitation; $CuFeS_2$; Fenton-like reaction; degradation; environmental water samples

Citation: Wen, P.-Y.; Lai, T.-Y.; Wu, T.; Lin, Y.-W. Hydrothermal and Co-Precipitated Synthesis of Chalcopyrite for Fenton-like Degradation toward Rhodamine B. *Catalysts* **2022**, *12*, 152. https://doi.org/10.3390/catal12020152

Academic Editor: Roberto Fiorenza

Received: 31 December 2021
Accepted: 25 January 2022
Published: 26 January 2022

1. Introduction

Since the industrial revolution, the development of various industries has made life in human society more convenient, but has also caused many environmental problems. Wastewater, such as cooling water and clean water for equipment, is discharged from various industrial processes. The constituents in any wastewater are diverse and complex consisting of raw materials, intermediate products, by-products, and end products. Charging these compounds directly to the environment can have detrimental consequences. For example, oxygen-containing organic compounds such as aldehydes, ketones, and ethers are reductive, meaning that they are capable of consuming dissolved oxygen in the water to a low-level endangering aquatic organisms. Wastewater can also contain a large amount of nitrogen, phosphorus, and potassium which can promote the growth of algae and triggering eutrophication pollution in water bodies [1]. Released toxic substances from wastewater can bio-accumulate in fish and eventually pass to people who consumed it. Thus, wastewater treatment is an important process to avoid these consequences. Within the treatment options, physical, biological, and chemical methods are mainly used to treat wastewater by removing pollutants in the water and reducing organic pollutants and eutrophic substances in the water [2–8].

Among many treatment processes, the in-site chemical oxidation method is to inject and mix oxidants into the underground environment aiming to degrade pollutants

in groundwater and soil [9–11]. Under ideal conditions, this chemical treatment can convert organic pollutants into less toxic molecules, such as carbon dioxide, water, and inorganic salts. The commonly used oxidants are permanganate (MnO_4^-), Fenton reagent (Fe^{2+}/H_2O_2), and ozone (O_3) [12–15]. The mechanism of Fenton reagent (Fe^{2+}/H_2O_2) in reactions has been known to produce •OH radicals, which can cleave C–H bonds of organic compounds, turning them into environmentally benign final products [16,17]. However, this Fenton method has some drawbacks including the specific pH working range and Fe sludge precipitation at the end of the Fenton reaction [18,19]. Another alternative way to generate radicals with a wider pH working range is by using persulfate salts [20–26]. Persulfate salts can come from two types: peroxymonosulfate (HSO_5^-) and peroxydisulfate ($S_2O_8^{2-}$), both of which contain an O–O bond (peroxide group) capable of generating $\bullet SO_4^-$ radicals and •OH radicals in Fenton-like reaction for degradation of organic compounds [27,28]. Persulfate salts are strong oxidant (E^0 = 2.1 V), yet they are very stable for transportation and prolong storage making them very attractive oxidants for underground water treatment [29].

There are a few ways of activating persulfate to generate radicals, such as thermal decomposition, alkaline activation, transition metal ions activation, and heterogeneous catalysis [30]. Among them all, transition metal ions activation is considered the simplest and most benign method with no external energy requirement and recyclability of transition metal ions [31–34]. Cobalt ions are commonly used in activating persulfate in research, but their hazardous nature makes them unsuitable for water treatment [35,36]. Thus, it is necessary to find an alternative transition metal catalyst that can be used in water treatment.

Recently, Cu/Fe-bearing solids such as chalcopyrite ($CuFeS_2$) have been widely used as catalysts in advanced oxidation processes (AOPs) for wastewater treatment [37–41]. For instance, Dotto et al. demonstrated the ability of their prepared citrate-$CuFeS_2$ materials to degrade 90% of bisphenol A (BPA) in a 15-min Fenton process [42]. Their novel $CuFeS_2$ samples were prepared with a microwave reactor (1400 W, 200 °C, 7 min). Pastrana-Martinez et al. used the mineral of $CuFeS_2$ mined from Jendouba, Tunisia, to catalyze tyrosol degradation (85.0% degradation within 60 min) by using a UV light-assisted Fenton reaction [43]. However, for ground water treatment, this method requires UV light as external energy requirement. Chang et al. proposed that the microwave-assisted synthesis of $CuFeS_2/Ag_3PO_4$ with enhanced rhodamine B (RhB) degradation (96% degradation within 1 min) under visible light-Fenton process [44]. However, these methods also need light irradiation to improve the degradation performance of $CuFeS_2$.

Herein, we synthesized $CuFeS_2$ samples through hydrothermal and co-precipitated method to realize the advantages in material preparation, stability of materials, and degradation performance in new water treatment option. We expected higher temperature and pressure treatment (hydrothermal process) to make the prepared particles with small size and high special surface area compared to the co-precipitated process, resulting in higher catalytic activity [45–47]. In order to prove this, the prepared $CuFeS_2$ samples in the presence of $Na_2S_2O_8$ were used to evaluate the degradation efficiency of various dyestuff (RhB, rhodamine 6G [R6G], methylene blue [MB], methyl orange [MO], and BPA). The degradation mechanism of $CuFeS_2$ was elucidated and the reactive species were identified. Finally, the practical applications of $CuFeS_2$ samples in the treatment of environmental samples were demonstrated.

2. Results and Discussion

2.1. Characterization of the $CuFeS_2$ Samples

The morphology and composition of the prepared H-$CuFeS_2$ and C-$CuFeS_2$ samples were analyzed through SEM and EDS-mapping (Figure 1). As shown in Figure 1, H-$CuFeS_2$ and C-$CuFeS_2$ samples appear as sphere-like structures, with the average diameter ranging 25–40 nm and 95–125 nm, respectively. The smaller particle size of the H-$CuFeS_2$ samples can be the result of hydrothermal treatment which hindered the particle growth. On the other hand, high concentration of $N_2H_4 \cdot H_2O$ was used as reducing agent to prepare

C-$CuFeS_2$ samples, resulting in particle agglomeration. In addition, Ostwald ripening may occur during heating procedure. Therefore, small C-$CuFeS_2$ samples dissolved and redeposited onto larger C-$CuFeS_2$ samples. From the results of energy dispersive spectrometer (EDS)-mapping (green color, S elements; blue color, Fe elements; and red color, Cu elements), the presence of Cu, Fe, and S elements in both $CuFeS_2$ samples were confirmed and dispersed well in their crystals.

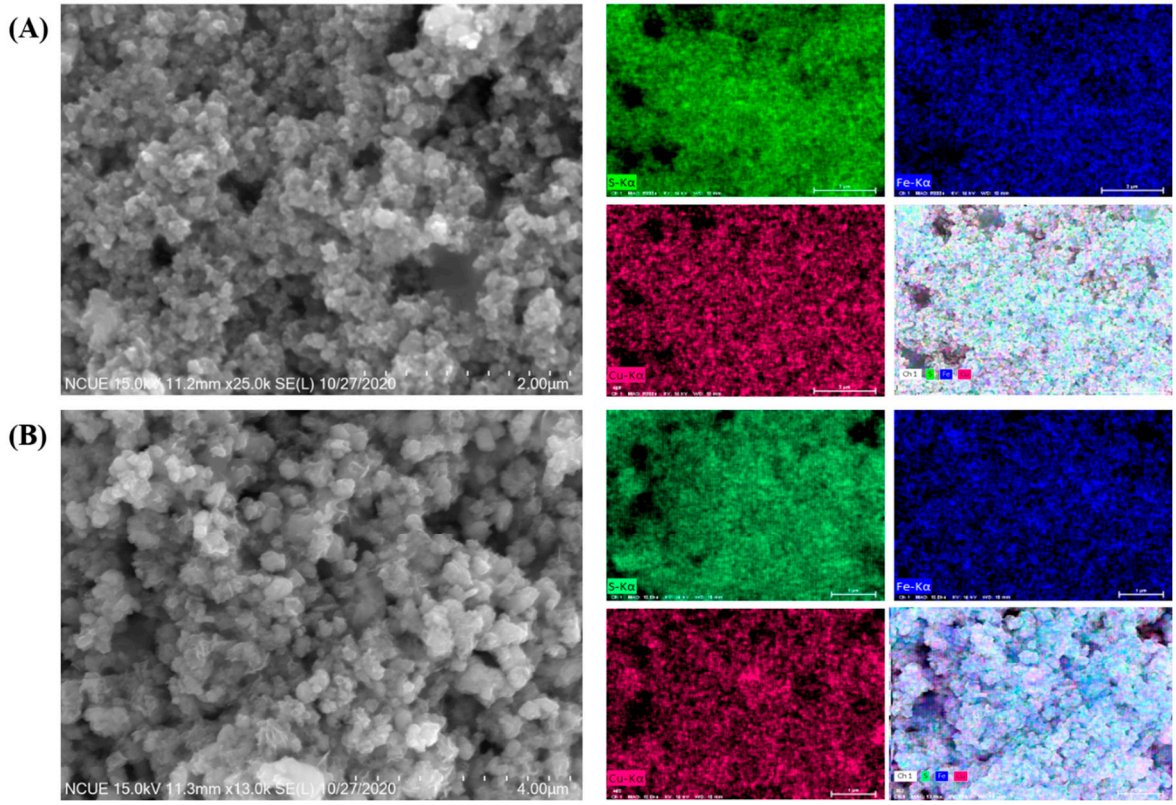

Figure 1. SEM images and EDS-mapping of (**A**) H-$CuFeS_2$ and (**B**) C-$CuFeS_2$ samples.

Figures 2 and 3 showed the TEM images and EDS spectra of the $CuFeS_2$ samples. The diameters of both $CuFeS_2$ samples from TEM images were consistent with the SEM results. We also found both $CuFeS_2$ samples possessed 0.31 nm and 0.23 nm of lattice lines, corresponding to the crystal planes of (112) and (204). The EDS spectra of the prepared $CuFeS_2$ samples confirm the presence of Cu, Fe, and S elements in their crystals, accordingly. The atomic ratios (Cu:Fe:S) for the H-$CuFeS_2$ and C-$CuFeS_2$ samples were determined to be 1.1:1:1.8 and 1.4:1:2.0, respectively. High content of Cu elements in the C-$CuFeS_2$ in the sample is consistent with lower solubility predicted from smaller Ksp value of Cu_2S when comparing with Fe_2S_3 (Ksp of Fe_2S_3: 3.7×10^{-19}, Ksp of Cu_2S: 2.0×10^{-47}).

XRD was used to investigate the crystal structure of the prepared $CuFeS_2$ samples. The XRD patterns of the prepared $CuFeS_2$ samples are shown in Figure 4A. The diffraction peaks at 29.5°, 49.1°, and 58.6° were identified and assigned to the (112), (204), (312), (204), and (312) faces of the tetragonal chalcopyrite $CuFeS_2$, respectively (PDF 83-0983). Through the Scherrer equation, the average crystal size of H-$CuFeS_2$ and C-$CuFeS_2$ was 20.36 and 11.2 nm, respectively. The Raman spectra of the prepared $CuFeS_2$ samples are shown in Figure 4B. The Raman shifts at 212 cm^{-1}, 276 cm^{-1}, and 379 cm^{-1} correspond to the S element, Cu(I)-S, and Fe(III)-S stretching vibration, respectively.

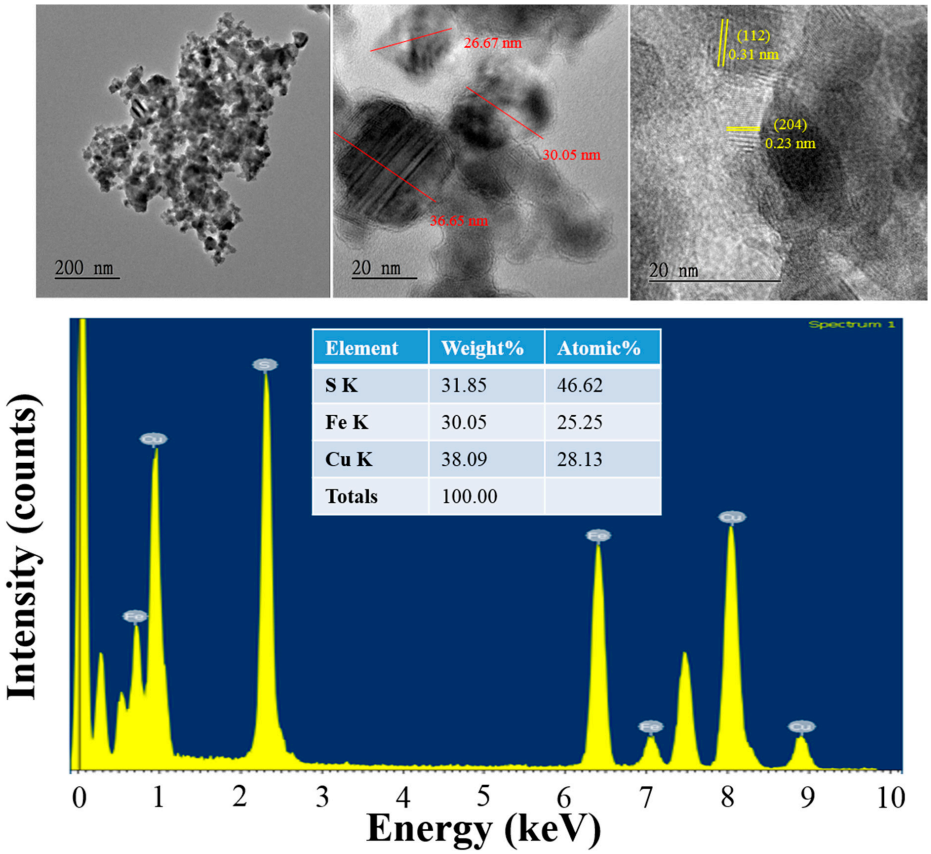

Figure 2. TEM images and EDS spectra of H-$CuFeS_2$ samples.

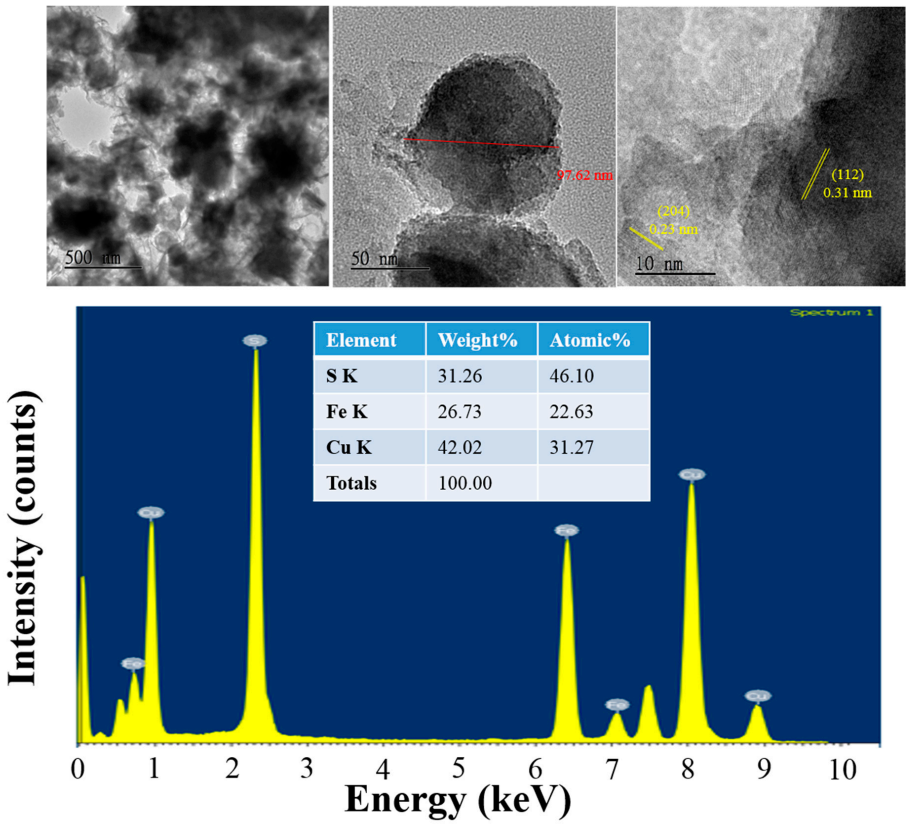

Figure 3. TEM images and EDS spectra of C-$CuFeS_2$ samples.

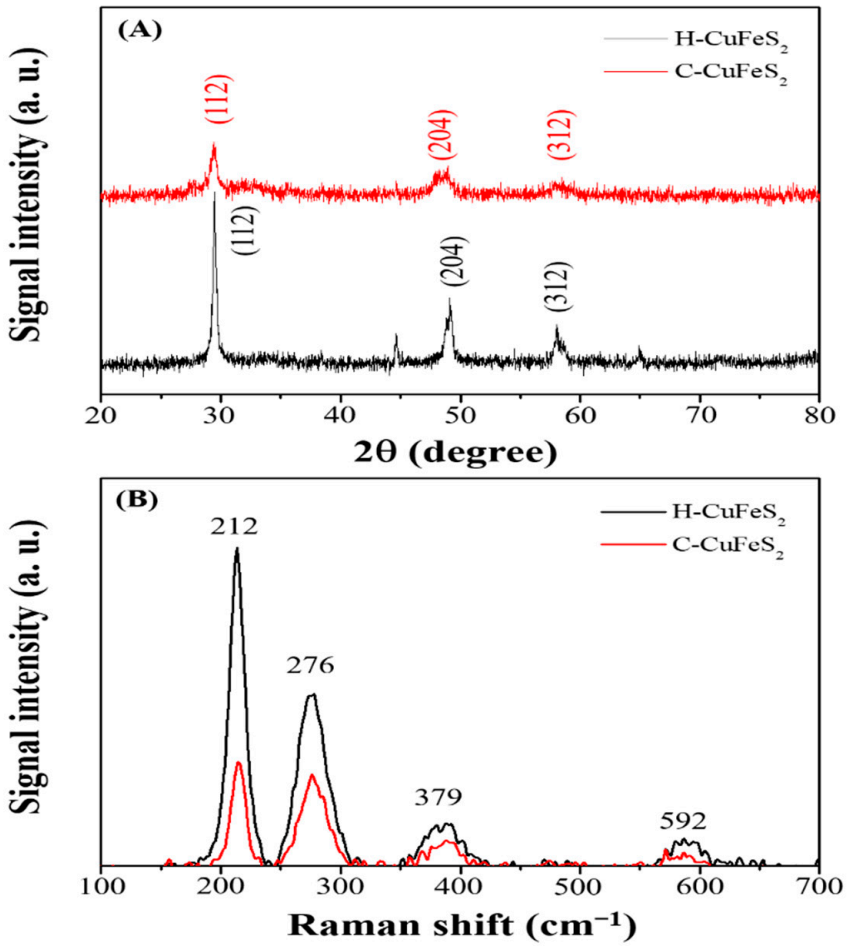

Figure 4. (**A**) XRD and (**B**) Raman spectra of H-$CuFeS_2$ (black), and C-$CuFeS_2$ (red) samples.

As another quality assurance method, XPS analysis of the prepared $CuFeS_2$ samples (Figures 5 and 6) revealed that it contains three elements: Cu, Fe, and S [48,49]. High-resolution XPS revealed Cu2p, Fe2p, and S2p in the H-$CuFeS_2$ samples as shown in Figure 5B–D, respectively. In Figure 5B, the peaks at 931.9 and 951.7 eV correspond to Cu^{+} $2p_{3/2}$ and Cu^{+} $2p_{1/2}$, respectively, whereas those at 933.2 and 953.0 eV correspond to Cu^{2+} $2p_{3/2}$ and Cu^{2+} $2p_{1/2}$, respectively. The peaks at 711.7 and 724.9 eV correspond to Fe^{2+} $2p_{3/2}$ and Fe^{2+} $2p_{1/2}$, respectively, whereas those at 715.2 and 734.3 eV correspond to Fe^{3+} $2p_{3/2}$ and Fe^{3+} $2p_{1/2}$, respectively (Figure 5C). The peaks at 162.5 and 167.8 eV correspond to S^{2-} 2p and S^{6+} 2p, respectively (Figure 5D). For C-$CuFeS_2$ samples, the peaks at 931.9 and 951.6 eV correspond to Cu^{+} $2p_{3/2}$ and Cu^{+} $2p_{1/2}$, respectively, whereas those at 934.1 and 952.7 eV correspond to Cu^{2+} $2p_{3/2}$ and Cu^{2+} $2p_{1/2}$, respectively (Figure 6B). The peaks at 711.4 and 724.8 eV correspond to Fe^{2+} $2p_{3/2}$ and Fe^{2+} $2p_{1/2}$, respectively, whereas those at 714.6 and 734.2 eV correspond to Fe^{3+} $2p_{3/2}$ and Fe^{3+} $2p_{1/2}$, respectively (Figure 6C). The peaks at 162.5 and 168.9 eV correspond to S^{2-} 2p and S^{6+} 2p, respectively (Figure 6D).

According to its peak area, the percentage of different oxidation states of each element in the prepared $CuFeS_2$ samples can be estimated. In H-$CuFeS_2$ samples, elemental compositions were found 82.3% Cu^{+} and 17.6% Cu^{2+} from Cu analysis, 66.9% Fe^{2+} and 33.1% Fe^{3+} from Fe analysis, and 74.2% S^{2-} and 25.7% S^{6+} from sulfur analysis. In C-$CuFeS_2$ samples, elemental composition was found to be 90.6% Cu^{+} vs. 9.3% Cu^{2+} for Cu, 60.8% Fe^{2+} vs. 39.2% Fe^{3+} for Fe, and 62.6% S^{2-} vs. 37.3%. S^{6+} for S.

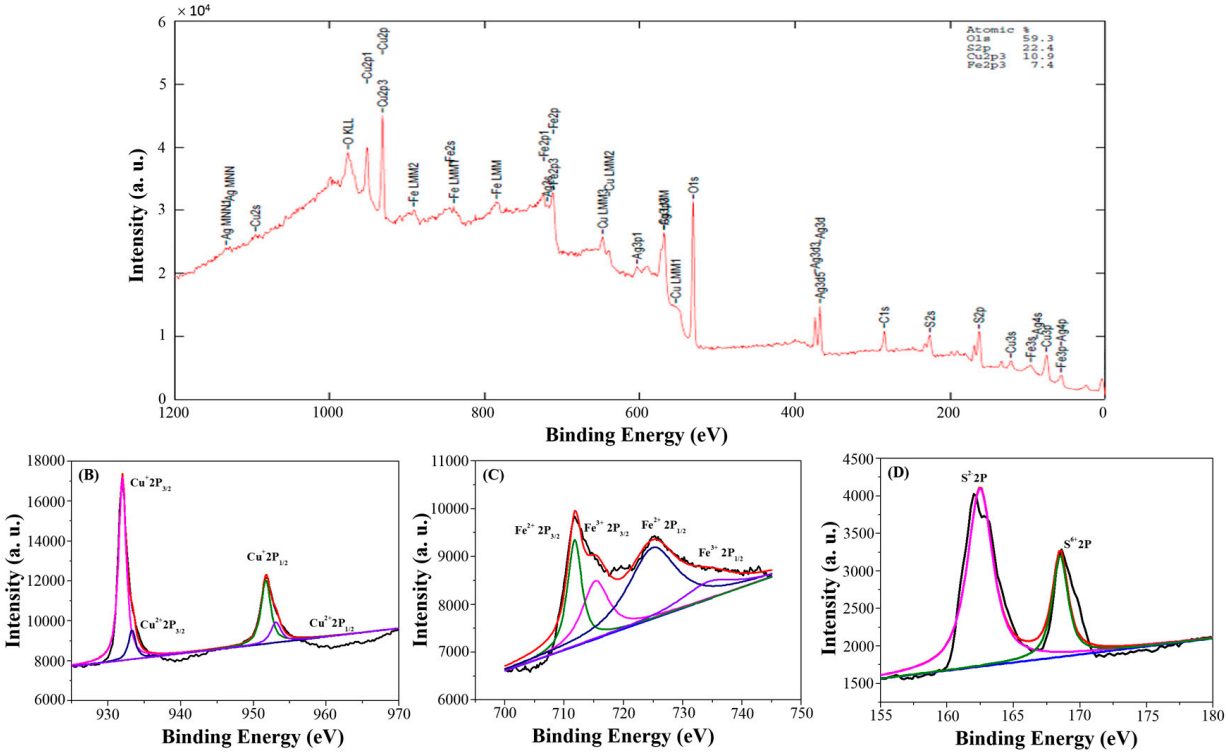

Figure 5. XPS spectra of H-$CuFeS_2$ samples: (**A**) full scan, (**B**) Cu_{2p}, (**C**) Fe_{2p}, and (**D**) S_{2p}.

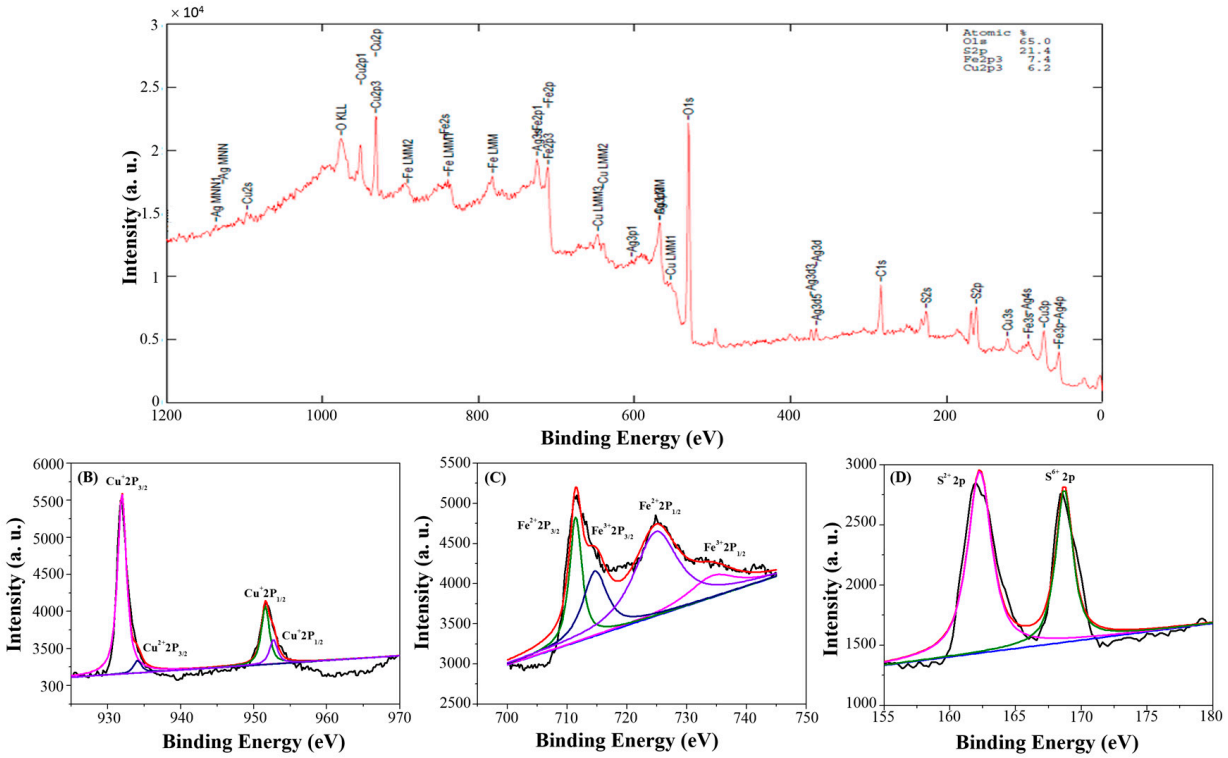

Figure 6. XPS spectra of C-$CuFeS_2$ samples: (**A**) full scan, (**B**) Cu_{2p}, (**C**) Fe_{2p}, and (**D**) S_{2p}.

2.2. Degradation Performance of the $CuFeS_2$ Samples

The degradation activity of the prepared $CuFeS_2$ samples was evaluated with RhB (20 ppm) first. According to our previous experience, the degradation efficiency decreased with an increasing dye concentration. This is because the excessive coverage of dye on

the active surface of catalysts leads to a decrease in the catalytic activity. Thus, 20 ppm RhB was selected for the experiment. The variations in the RhB concentration (C/C_0), where C_0 is the initial RhB concentration, and C is the RhB concentration at time t, with the reaction time for the prepared $CuFeS_2$ samples in the presence of H_2O_2 (Fenton reaction) and $Na_2S_2O_8$ (Fenton-like reaction), were found in Figure 7. Prior to the addition of the oxidant, each catalyst (0.20 g) was introduced to the 20 ppm RhB solution for 30 min in the dark (indicated as "−30 min" in Figure 7) to reach equilibrium. The RhB concentration for H-$CuFeS_2$ samples after this equilibration time is lower than that of C-$CuFeS_2$ samples, reflecting RhB adsorption on H-$CuFeS_2$ samples. This is because smaller size of the H-$CuFeS_2$ samples had higher specific surface area than C-$CuFeS_2$ samples. Through the Fenton reaction, the degradation efficiency within 30 min was 32.3% and 26.4% for the H-$CuFeS_2$ and C-$CuFeS_2$ samples, respectively (black and blue curve). This suggests that the degradation performance of H-$CuFeS_2$ is better than that of C-$CuFeS_2$, attributable to adsorption ability of high specific surface area for the H-$CuFeS_2$ samples. The results of RhB degradation through a Fenton-like reaction by the H-$CuFeS_2$ and C-$CuFeS_2$ samples were shown in the red and pink curve. The degradation efficiency within 30 min reaction time follows this order: H-$CuFeS_2$ (93.7%) > C-$CuFeS_2$ (66.3%), indicating H-$CuFeS_2$ having higher catalytic activity to produce $\bullet SO_4^-$ radicals. Furthermore, we found that degradation performance of $\bullet SO_4^-$ radicals is higher than that of •OH radicals for both $CuFeS_2$ samples. This is because of the different lifetimes of radicals ($\bullet SO_4^-$ radicals: 4 s, •OH radicals: 1 μs). Thus, the degradation system of H-$CuFeS_2$ through a Fenton-like reaction was selected for the further study.

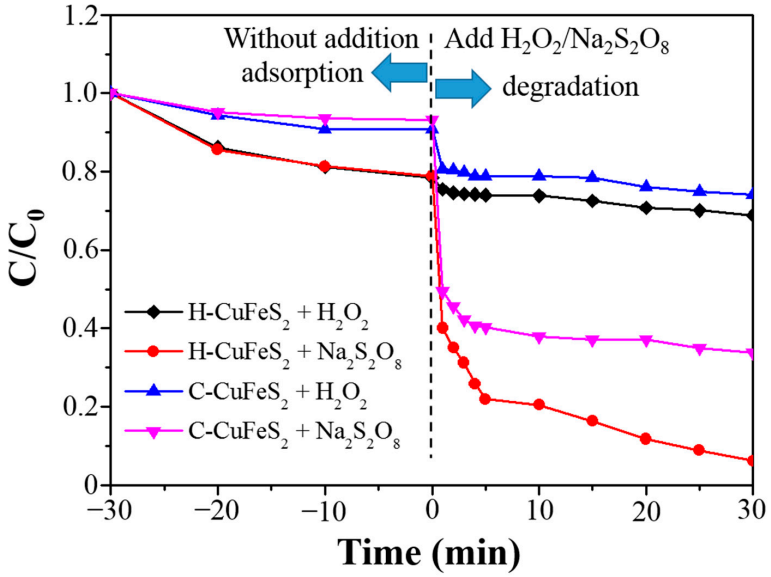

Figure 7. Fenton and Fenton-like reactions for RhB degradation at different conditions: H-$CuFeS_2$ in the presence of H_2O_2 (black), H-$CuFeS_2$ in the presence of $Na_2S_2O_8$ (red), C-$CuFeS_2$ in the presence of H_2O_2 (blue), and C-$CuFeS_2$ in the presence of $Na_2S_2O_8$ (pink).

To maximize the degradation performance of H-$CuFeS_2$, the effect from various concentrations of $Na_2S_2O_8$ was studied. As shown in Figure 8, the degradation efficiency increased with increasing $Na_2S_2O_8$ concentration. Due to low solubility of $Na_2S_2O_8$, we selected 4.0 mM of $Na_2S_2O_8$ as the optimum required concentration of $Na_2S_2O_8$. Dye adsorption on H-$CuFeS_2$ was observed in the absence of $Na_2S_2O_8$ (black cure in Figure 9). Although direct degradation of RhB by $Na_2S_2O_8$ without H-$CuFeS_2$ was noticed from the experiment due to the high oxidizing strength of $Na_2S_2O_8$ (red curve in Figure 9), its rate of degradation cannot compete with H-$CuFeS_2$ samples in the presence of $Na_2S_2O_8$, which achieved an impressive 98.8% within 10 min (blue cure in Figure 9). In addition, we also analyzed the degradation performances of Cu_2S and FeS_2 nanoparticles to investigate which

element is important for a Fenton-like reaction. As shown in Figure 10, the RhB degradation efficiency within 15 min reaches 64.1% and 89.0% for Cu_2S and FeS nanoparticles, respectively. These results suggested that the FeS_2 nanoparticles catalyze $Na_2S_2O_8$ to produce $\bullet SO_4^-$ radicals better than Cu_2S nanoparticles, indicating Fe component is important than Cu component for the Fenton-like reaction.

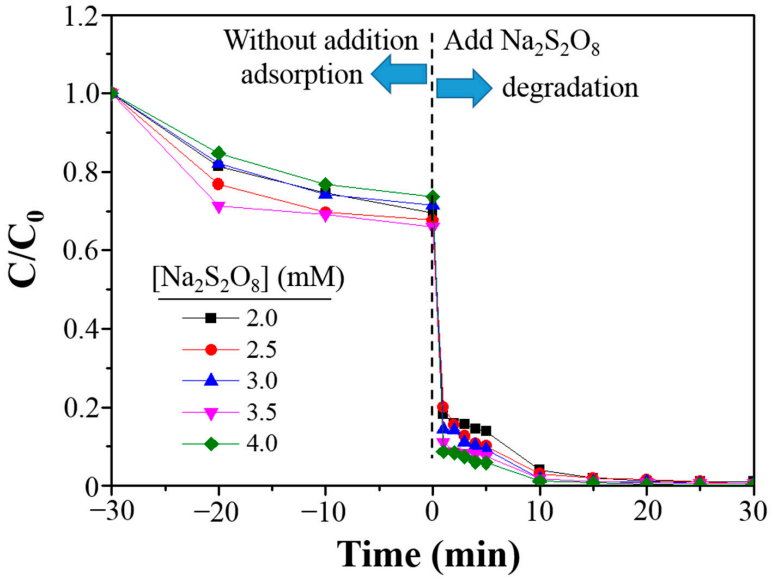

Figure 8. Fenton-like reaction for RhB degradation by H-$CuFeS_2$ samples at different concentration of $Na_2S_2O_8$.

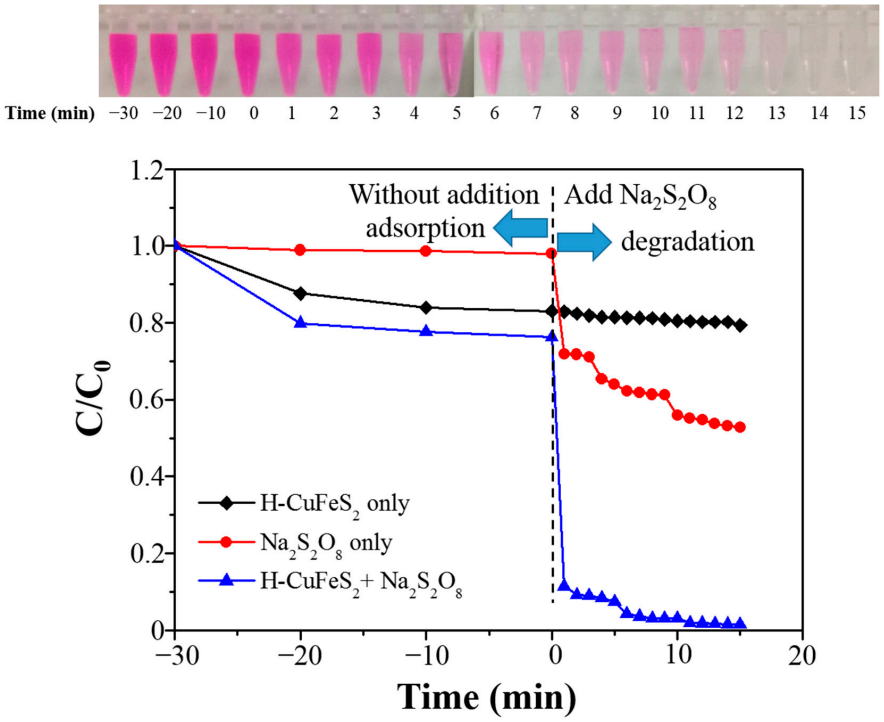

Figure 9. Fenton-like reaction for RhB degradation under different conditions: H-$CuFeS_2$ samples only (black), $Na_2S_2O_8$ only (red), and H-$CuFeS_2$ in the presence of $Na_2S_2O_8$ (blue). Top image: photographs of the RhB solution under the Fenton reaction at different reaction time.

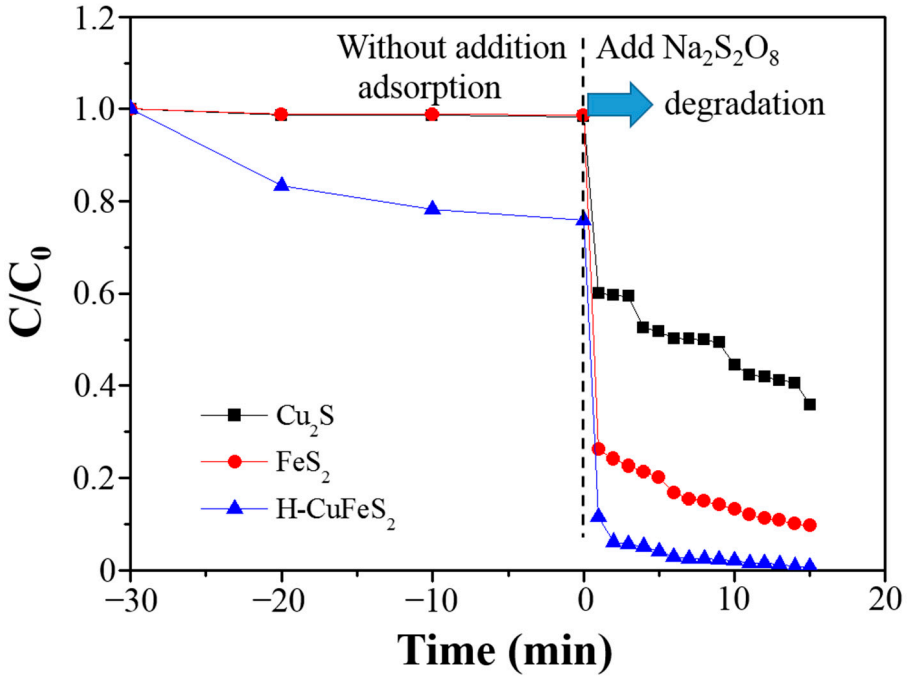

Figure 10. Fenton-like reaction for RhB degradation in the presence of $Na_2S_2O_8$ by using different catalysts: Cu_2S (black), FeS_2 (red), and H-$CuFeS_2$ (blue).

2.3. Degradation Mechanism of H-$CuFeS_2$

As a key mechanistic study, the active species involved in the degradation reaction were identified systematically using the free radical trapping experiments (Figure 11A). Methanol and NaN_3 were used as •OH and $•SO_4^-$ scavengers, respectively. Comparing to methanol, NaN_3 inhibit RhB degradation more, indicating that $•SO_4^-$ radicals are the major species involved in the Fenton-like degradation (blue curve in Figure 11A). According to the results of the scavenger test and XPS experiment, we propose a possible degradation mechanism. First, Fe^{2+}/Cu^+ ions on the $CuFeS_2$ surface catalyzed $S_2O_8^{2-}$ to produce $•SO_4^-$ radicals (Equations (1) and (2)). Due to high oxidation activity of $•SO_4^-$ radicals (E^0 = 2.5–3.1 V), they were utilized to degrade dyes and to oxidize Fe^{2+}/Cu^+ ions (Equations (3)–(5)). Then, •OH radicals also produced from the oxidation reaction between $•SO_4^-$ radicals and H_2O/OH^- to degrade the dyes (Equations (6)–(8)). Thus, after adding methanol to the reaction mixture, RhB degradation in $CuFeS_2$ samples was slightly decreased, indicating that production of •OH radicals are considered as the indirect active species in the $CuFeS_2$ catalyzed RhB degradation (red curve in Figure 11A).

$$Fe^{2+} + S_2O_8^{2-} \rightarrow Fe^{3+} + •SO_4^- + SO_4^{2-} \quad (1)$$

$$Cu^+ + S_2O_8^{2-} \rightarrow Cu^{2+} + •SO_4^- + SO_4^{2-} \quad (2)$$

$$•SO_4^- + RhB \rightarrow CO_2 + H_2O \quad (3)$$

$$•SO_4^- + Fe^{2+} \rightarrow Fe^{3+} + SO_4^{2-} \quad (4)$$

$$•SO_4^- + Cu^+ \rightarrow Cu^{2+} + SO_4^{2-} \quad (5)$$

$$•SO_4^- + H_2O \rightarrow SO_4^{2-} + •OH + H^+ \quad (6)$$

$$•SO_4^- + OH^- \rightarrow SO_4^{2-} + •OH \quad (7)$$

$$•OH + RhB \rightarrow CO_2 + H_2O \quad (8)$$

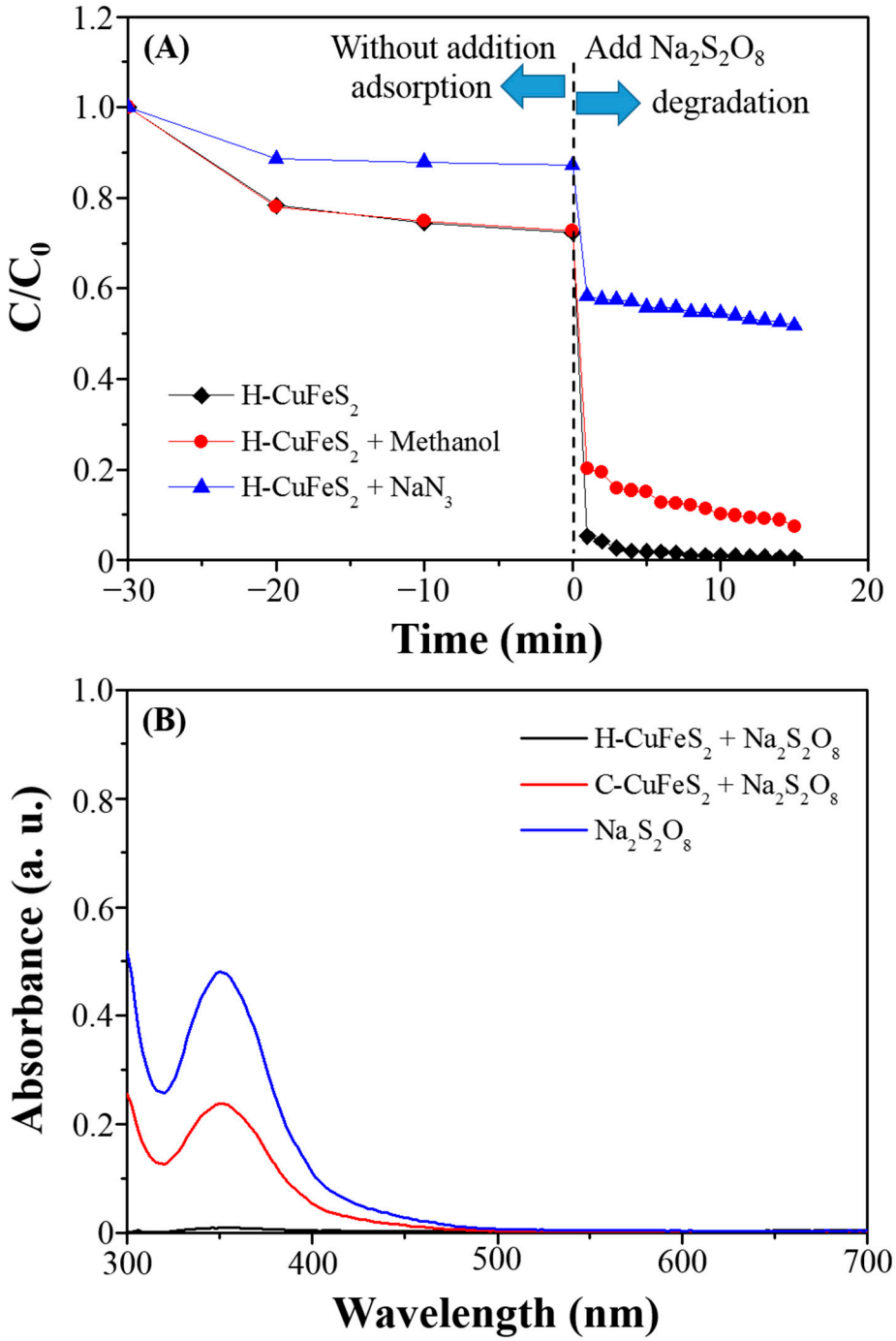

Figure 11. (**A**) Free radical trapping experiment and (**B**) absorbance spectra at different condition.

•SO_4^- radical production in the Fenton-like reaction was further studied using the spectrophotometric method [50]. According to Equations (9) and (10), I_3^- solution (light yellow) was found from chemical reaction between $S_2O_8^{2-}$ and KI. The absorbance spectra of the $S_2O_8^{2-}$/KI solution in the absence and presence of the prepared $CuFeS_2$ samples were evaluated. Figure 11B shows that an absorbance peak was observed at 358 nm for each sample and that the maximum absorbance was observed in the absence of the prepared $CuFeS_2$ samples (blue curve in Figure 11B). This suggests that $S_2O_8^{2-}$ produced the highest amount of I_2 compared to others, thereby leading to more chemical reactions with KI to generate I_3^-. Due to a high specific surface area and high content of Fe^{2+} ions, H-$CuFeS_2$ effectively catalyzed $S_2O_8^{2-}$ to produce •SO_4^- radicals, as a result of a few I_2 production. Thus, the absorbance intensity at 358 nm of H-$CuFeS_2$/$S_2O_8^{2-}$/KI mixing solution (black

curve in Figure 11B) was lower than that of C-$CuFeS_2$/$S_2O_8^{2-}$/KI mixing solution (red curve in Figure 11B).

$$S_2O_8^{2-} + 2I^- \rightarrow 2SO_4^{2-} + I_2 \quad (9)$$

$$I_2 + KI \rightarrow I_3^- + K^+ \quad (10)$$

On the basis of the results described above, the degradation scheme of the H-$CuFeS_2$ samples in the Fenton-like reaction was proposed (Scheme 1). •SO_4^- radicals and •OH radicals were produced from the Fenton-like reaction between $S_2O_8^{2-}$ and Fe^{2+}/Cu^+ ions on the H-$CuFeS_2$ surface to degrade RhB (Equations (1)–(8)). Then, Fe^{2+}/Cu^+ ions were regenerated through a series reduction of S^{2-} anions (Equations (11)–(13)). Moreover, it is also possible to produce Fe^{2+} ions by reduction reaction between Cu^+ and Fe^{3+} ions (Equation (14)).

$$S^{2-} + Fe^{3+}/Cu^{2+} \rightarrow Fe^{2+}/Cu^+ + S_2^{2-} \quad (11)$$

$$S_2^{2-} + Fe^{3+}/Cu^{2+} \rightarrow Fe^{2+}/Cu^+ + S_n^{2-} \quad (12)$$

$$S_n^{2-} + Fe^{3+}/Cu^{2+} \rightarrow Fe^{2+}/Cu^+ + SO_4^{2-} \quad (13)$$

$$Cu^+ + Fe^{3+} \rightarrow Fe^{2+} + Cu^{2+} \quad (14)$$

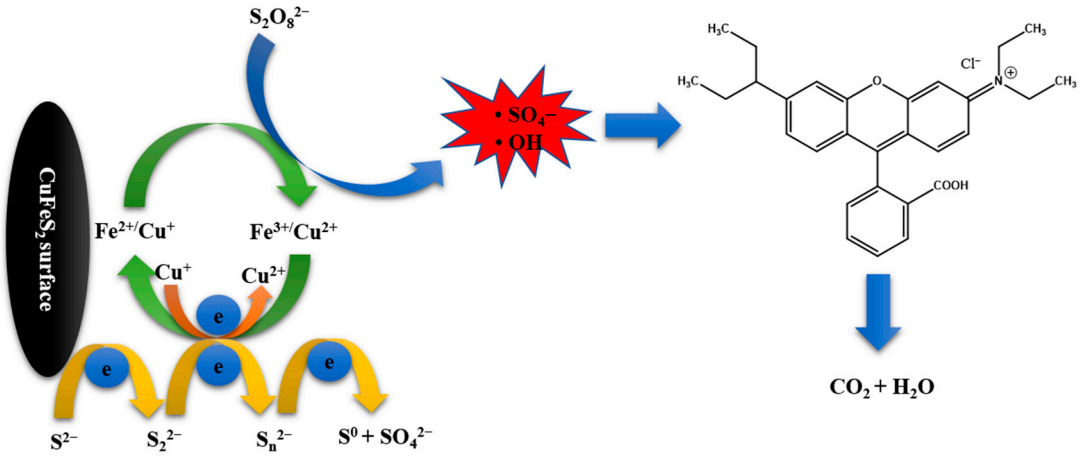

Scheme 1. Possible scheme of Fenton-like reaction for the H-$CuFeS_2$ samples.

2.4. Stability and Practical Applications of H-$CuFeS_2$

The stability of the catalyst is an essential parameter for the development of practical water treatment applications. To investigate the stability of H-$CuFeS_2$, results of pH effect, copper ions effect, and cyclic RhB degradation tests were evaluated as shown in Figures 12–14. Figure 12 showed the study of pH effect. RhB degradation by H-$CuFeS_2$ at pH 4.0 maintained a similar degradation efficiency at pH 7.0 (98.48% at pH 4.0 and 98.49% at pH 7.0, respectively), whereas that at pH 10.0 resulted in a considerable loss of efficiency (72.13% at pH 10.0). This is because most •SO_4^- radicals were converted to •OH radicals at alkaline condition (Equations (6)–(8)). Thus, •OH radicals are the major active radicals involved in dye degradation at alkaline condition. In addition, inactive porphyrin ferryl complexes (FeO^{2+}) are formed as Fe^{2+} ions in the alkaline solution. As a result, a weakened degradation result at pH 10.0 was found (Figure 12).

In the study of copper ion effect as shown in Figure 13, RhB degradation efficiencies by H-$CuFeS_2$ in the presence of Cu^+ ioins were 88.64% at pH 4.0, 91.21% at pH 7.0, and 87.42% at pH 10.0, whereas those in the presence of Cu^{2+} ions were 93.96% at pH 4.0, 94.21% at pH 7.0, and 91.19% at pH 10.0. Comparing to that at pH 10.0 in the absence of copper ions, an obvious improvement was found. This is because •SO_4^- radicals are produced in the presence of Cu^+ ions (Equation (2)). In addition, Fe^{2+}/Cu^+ ions were regenerated through reduction between S^{2-} anions and Fe^{3+}/Cu^{2+} ions (Equations (11)–(13)). As a result, an improve degradation at pH 10.0 was found.

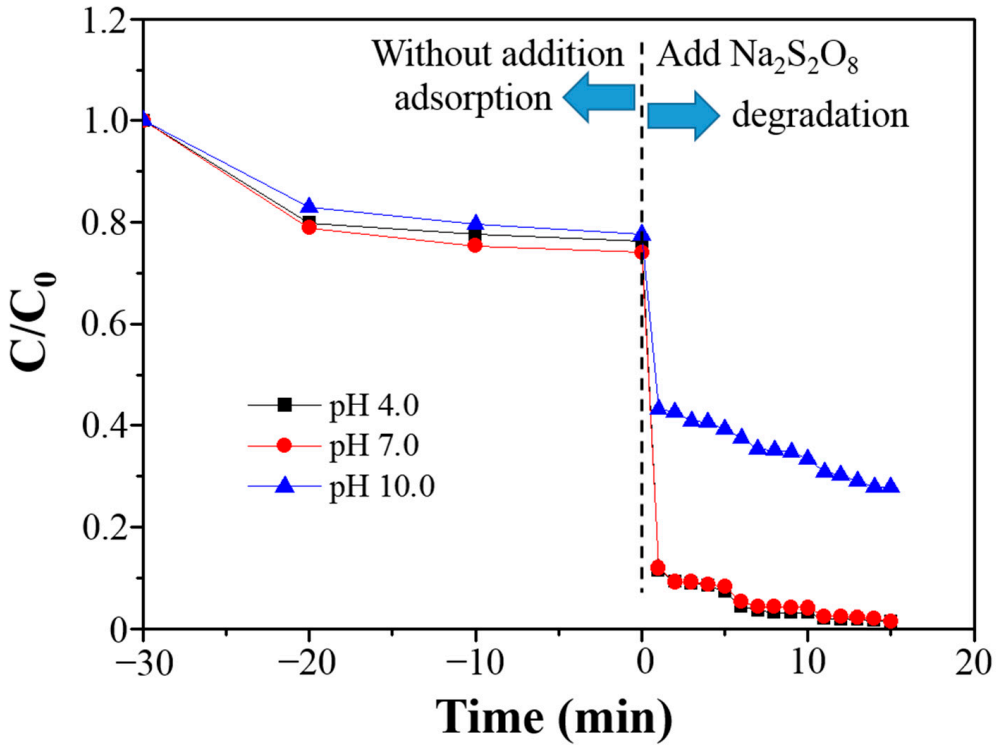

Figure 12. Fenton-like reaction for RhB degradation by the H-$CuFeS_2$ samples at different pH value system.

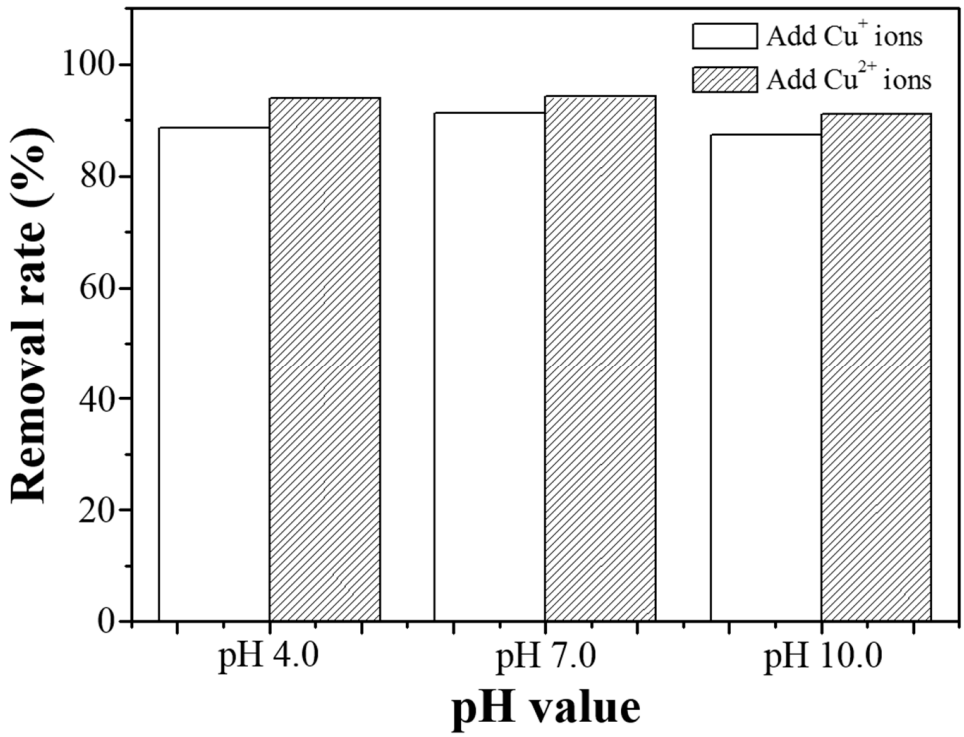

Figure 13. RhB degradation efficiency by the H-$CuFeS_2$ samples at different pH value system in the presence of copper ions.

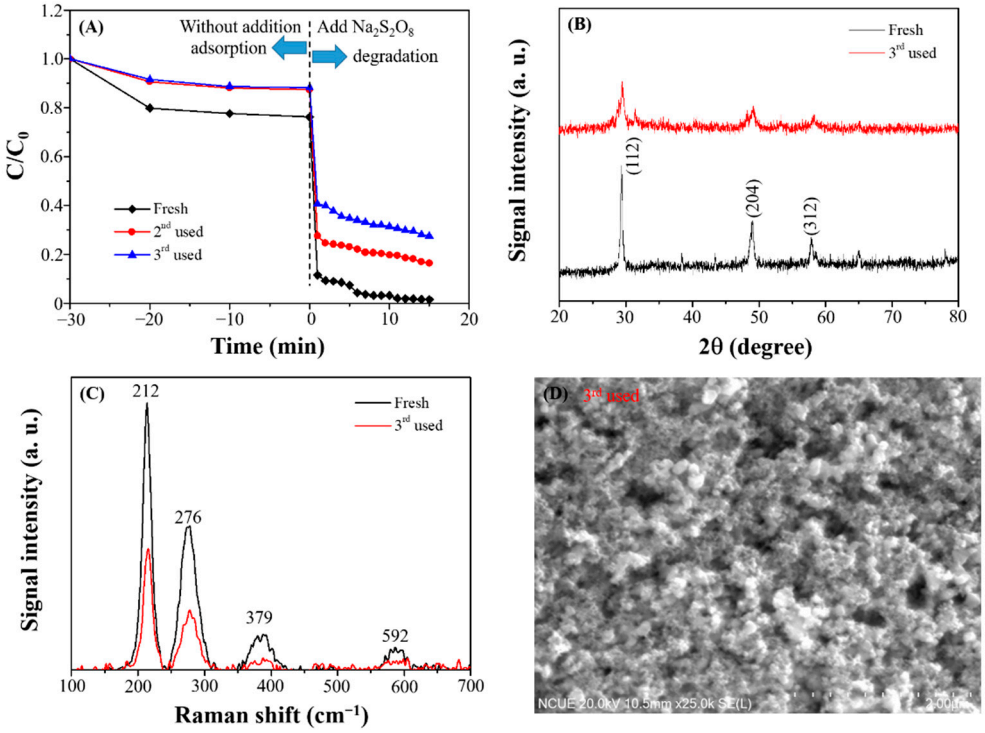

Figure 14. (**A**) Fenton-like reaction for RhB degradation by the H-$CuFeS_2$ samples for the recycling -used test, (**B**) XRD, (**C**) Raman spectra, and (**D**) SEM image of the 3rd used samples.

For recyling-used study, Figure 14A showed RhB degradation by H-$CuFeS_2$ exhibited a considerable loss of efficiency (from 98.48% to 72.46% after three cycles). Furthermore, the corresponding XRD, Raman, and SEM results (Figure 14B–D) suggest a decrease in the phase structure of the H-$CuFeS_2$ samples after the repeated reactions, indicating the destruction of the H-$CufeS_2$ sample crystalization. In addition, EDS spectrum found that the atomic ratio (Cu:Fe:S) for the third used H-$CuFeS_2$ samples was determined to be 1:1:1.9. The morphology of the third used samples still retained sphere-like structures, with the average diameter ranging 20–35 nm. Further research to improve recycling-used ability by other heterojunction, such as those doped by Ag@Ag_3PO_4 nanoparticles, is now underway in our laboratory.

To assess the practical applications of H-$CuFeS_2$ as a new water treatment option, various dyes (R6G, MB, and MO) and colorless organic compound (BPA) were tested (Figure 15A). H-$CuFeS_2$ exhibited excellent degradation efficiency toward R6G, MB, MO, and BPA, with 96.84%, 93.86%, 81.89%, and 75.24% degradation achieved within 10 min, respectively. In addition, the mineralization performance of H-$CuFeS_2$ comparing to a traditional Fenton reaction (Fe^{2+}/H_2O_2) was evaluated. From the TOC analysis (Figure 15B), mineralization efficiency for the Fe^{2+}/H_2O_2 and H-$CuFeS_2/S_2O_8^{2-}$ system was 70.0% and 80.1%, respectively, representing 10.1% improvement of RhB degradation. Finally, the prepared H-$CuFeS_2$ samples were used to degrade RhB in the environmental water samples (pond water and seawater). H-$CuFeS_2$ exhibited adequate mineralization efficiency through the Fenton-like reaction for RhB degradation. A notable difference in the mineralization efficiency for RhB was observed for the seawater samples (47.9% efficiency within 10 min) compared with pond water samples (63.8% efficiency within 10 min), probably because of the effect of higher concentration of anions or radical scavengers in the seawater sample that reduced the degradation activity of H-$CuFeS_2$. Nevertheless, the studies on the environmental water samples strongly support the benefits of this newly developed H-$CuFeS_2$-based Fenton-like water treatment option.

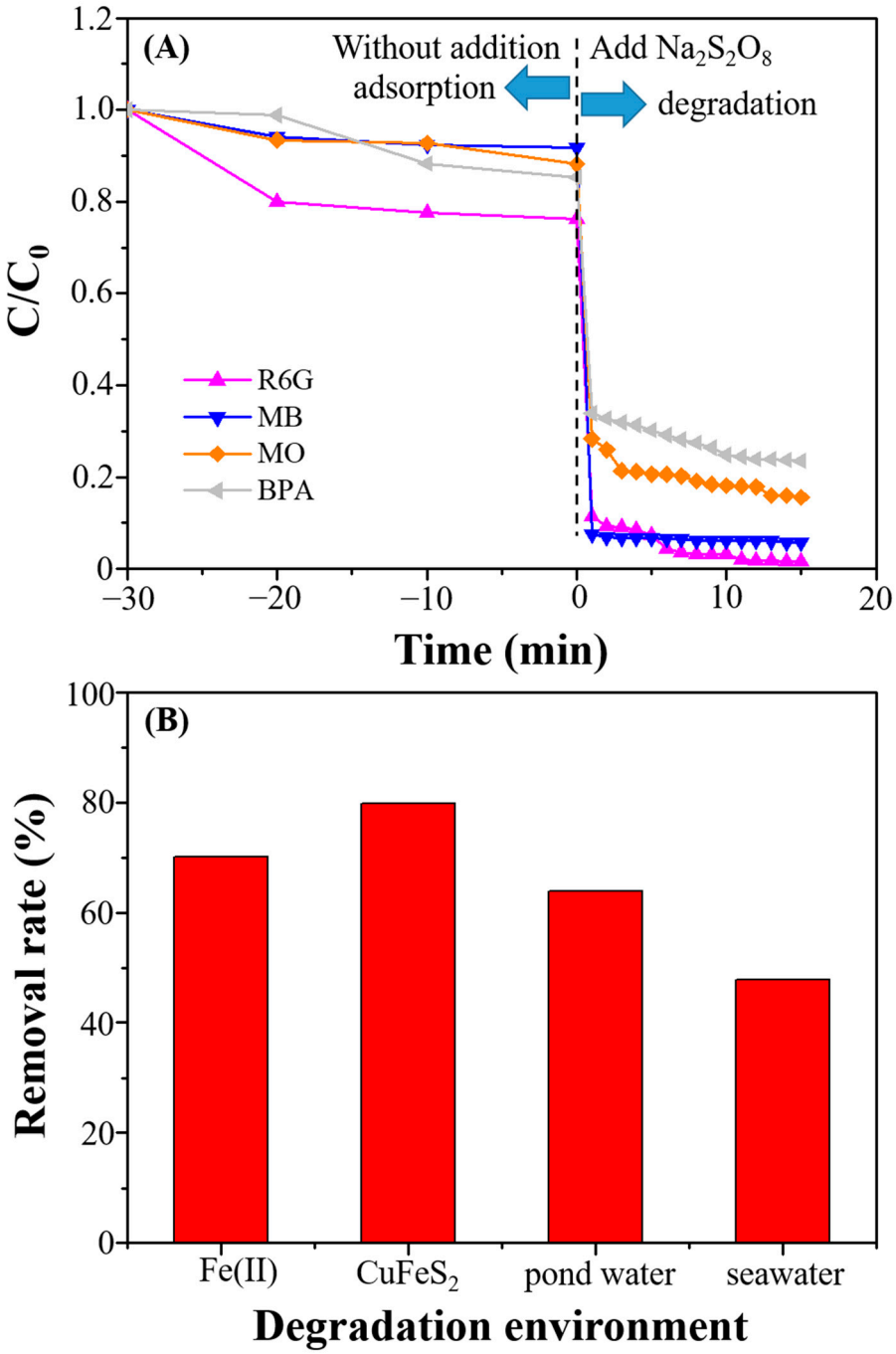

Figure 15. Fenton-like reaction of (**A**) different dyestuff by the H-$CuFeS_2$ samples, (**B**) TOC analysis of different degradation systems by using Fe(II) and the H-$CuFeS_2$ samples in the different environmental water samples.

3. Materials and Methods

3.1. Preparation of $CuFeS_2$

All chemicals were purchased from Sigma Aldrich (St. Louis, MO, USA) and were of analytical grade and used without further purification. In this study, hydrothermal (H) and co-precipitated method (C) were used to prepare $CuFeS_2$ samples, representing as H-$CuFeS_2$ and C-$CuFeS_2$, respectively. For hydrothermal procedure, 0.989 g of CuCl, and 2.703 g of $FeCl_3 \cdot 6H_2O$ were added to 57 mL of deionized water, with stirring for 10 min. Then, 8 mL of $Na_2S \cdot 9H_2O$ (0.02 mol) was added dropwisely into the above green mixture. After stirring for 30 min, the black mixture was transferred into a Teflon-lined stainless-steel

autoclave. The autoclave was sealed and heated in an electric oven at 200 °C for 10 h. After the autoclave naturally cooled to room temperature, the precipitates were centrifuged (5000 rpm, 15 min) and washed three times with ethanol and deionized water, and then dried in vacuum at 60 °C overnight. In addition, Cu_2S and FeS_2 nanoparticles were prepared following similar method without adding $FeCl_3 \cdot 6H_2O$ and CuCl precursor, respectively.

For the co-precipitated method, 4.95 mg of CuCl, and 0.0135 g of $FeCl_3 \cdot 6H_2O$ were added to 20 mL of deionized water, with stirring at 70 °C for 10 min. Then, 1 mL of NH_4OH (30%) and 1 mL of $N_2H_4 \cdot H_2O$ (64–65%) were added dropwise into the above mixture with stirring at 70 °C for 3 h. After that, 0.024 g of $Na_2S \cdot 9H_2O$ was added into the above brown mixture with stirring at 70 °C for 3 h. Finally, the black precipitates were centrifuged (5000 rpm, 15 min) and washed three times with ethanol and deionized water, and then dried in vacuum at 60 °C overnight.

3.2. Characterization of $CuFeS_2$

The morphological and compositional characteristics of all as-prepared samples were observed with scanning electron microscopy (SEM) on a HITACHI S-4300 (Hitachi, Tokyo, Japan) and transmission electron microscopy (TEM) on a 1200EX II (JEOL, Tokyo, Japan) equipped with a QUANTAX Annular XFlash QUAD FQ5060 (Bruker Nano, Berlin, Germany). The crystallographic texture of the samples was measured by powder X-ray diffraction (XRD) on SMART APEX II (Bruker AXS, Billerica, MA, USA) using Cu Kα radiation (λ = 1.5406 Å). Raman spectra were collected at room temperature using a confocal micro-Raman system (Thermo Scientific Inc., New York, NY, USA). A 532 nm laser line was used as the photoexcitation source with a laser power of 2 mW focused on the sample for 10 s. The binding energy of elements was determined through X-ray photoelectron spectroscopy (XPS) on a VG ESCA210 (VG Scientific, West Sussex, UK).

3.3. Degradation Procedure

RhB degradation was used to assess the degradation activity of the prepared samples. For the Fenton-like reaction, 20 mg of the prepared catalyst samples was added into the RhB solution (20 ppm, 50 mL), and the solution was stirred in the dark for 30 min. At 10 min before adding $Na_2S_2O_8$, the absorbance at its characteristic absorption peak of 550 nm was measured to check the adsorption ability of the prepared samples. Subsequently, 100 µL of $Na_2S_2O_8$ (2 M) was added to dye solution. After a given time interval, 1 mL of suspension was sampled with a plastic pipette and this aliquot was quenched immediately by adding 10 µL NaN_3 (1 M) and filtered by a 0.22-µm syringe filter organic membrane to remove catalyst particles. The concentration of RhB was measured using a Synergy H1 hybrid multimode microplate reader (BioTek Instruments, Winooski, VT, USA) at its characteristic absorption peak of 550 nm. Similar processes were performed for other catalysts (Cu_2S and FeS_2), dyestuffs (R6G, MB, and MO), and organic pollutant (BPA). After the experiment, TOC concentration was determined on an Elementar Acquray TOC analyzer (Elementar Analysensysteme GmbH, Langenselbold, Germany) to evaluate the extent of mineralization.

3.4. Free Radical Trapping Experiment

To investigate the active species generated during RhB degradation over H-$CuFeS_2$, the trapping experiment was conducted using NaN_3 and methanol (each 0.1 M) as the capturing agent for $\bullet SO_4^-$ radicals and •OH radicals, respectively. The implemented trapping experimental procedure was identical to the steps mentioned in the degradation section with an additional step of adding the capturing agent at each run.

4. Conclusions

The prepared H-$CuFeS_2$ samples showed higher RhB degradation efficiency through the Fenton-like reaction than the prepared C-$CuFeS_2$, FeS_2, Cu_2S nanoparticles, and previously reported samples (Table 1). This high enhancement in the degradation efficiency

(98.8% RhB degradation within 10 min) was attributed to the prepared H-$CuFeS_2$ samples possessed smaller size and higher surface area. Based on the results of scavenger test and radicals' quantitation experiments, H-$CuFeS_2$ catalyzed $Na_2S_2O_8$ to produce $\bullet SO_4^-$ radicals and •OH radicals for the organics degradation. As we know, the three limiting factors to address prior to industrial application were viable methods of catalyst preparation, the catalyst durability and universality under operating conditions. The prepared H-$CuFeS_2$ samples possessed several attractive features. First, the prepared H-$CuFeS_2$ samples in the presence of $Na_2S_2O_8$ had 98.8% RhB degradation performance within 10 min. In addition, various organics (R6G, MB, MO, and BPA) with 75.24–96.84% degradation efficiency could be achieved. However, the repeated use of H-$CuFeS_2$ showed performance deterioration due to the change in the crystal phase of used H-$CuFeS_2$. Further research on the high recycling-used ability of other heterojunction $CuFeS_2$ composites, such as those doped by $Ag@Ag_3PO_4$ nanoparticles, is now underway in our laboratory. Finally, the prepared H-$CuFeS_2$ samples were used to degrade RhB with 10.1% mineralization improvement comparing to traditional Fenton reaction (Fe^{2+}/H_2O_2). It is also easy to recover H-$CuFeS_2$ catalyst comparing to Fe^{2+} ions. In addition, H-$CuFeS_2$ catalyst deposited on a cellulose-based substrate is ongoing in our lab. The difficult separation and recycle of powder catalyst may result in high cost and secondary pollution, therefore, the powder form of catalyst greatly limited the commercial industrial application. More importantly, H-$CuFeS_2$ deposited on cellulose is very suitable for the dynamic-flow water treatment system. We will propose a new adsorption-degradation strategy for the pollutant removal in industrial level application in the future.

Table 1. Comparison of degradation performance using the (photo-) Fenton-like reaction.

Samples	Preparation	Degradation Performance	Target	Ref.
CuO/MSS	Hydrothermal method	90% degradation (0.15 g catalyst/50 ppm BPA) within 45 min	BPA	[20]
MMSS	Surface etching method	90% degradation (0.1 g catalyst/50 ppm MB) within 60 min	MB	[21]
Natural pyrite	Mined from Anhui, China	90% degradation (0.1 g catalyst/100 ppm MB) within 120 min	MB	[26]
$CDs/Fe_3O_4@CS$	Solvothermal method	96% degradation (0.3 g catalyst/50 μM Ibuprofen (IBP)) within 2 h (350-W Xe lamp)	IBP	[23]
TiO_2 nanotubes arrays	Anodization	94.6% degradation (1 ppm BPA) within 30 min (300-W Xe lamp)	BPA	[51]
$Fe^0@Fe_3O_4$ nanowires	Reduction method	100% degradation (2.5 mg catalyst/0.5 ppm Atrazine (ATZ)) within 6 min	ATZ	[24]
FeOCl nanosheets	Pyrolysis method	86.5% degradation (0.05 g catalyst/10 μM Phenacetin (PCNT)) within 30 min	PCNT	[25]
$CuFeS_2$	Hydrothermal method	98.8% degradation (0.02 g catalyst/20 ppm RhB) within 10 min	RhB, R6G, MB, MO, BPA	This study

In summary, this study discovered the hydrothermal synthesis of $CuFeS_2$ samples and successfully demonstrated the application of the Fenton-like reaction in the environmental

water samples. The current findings can be used to the application of AOPs in wastewater treatment in the future.

Author Contributions: Conceptualization, P.-Y.W. and Y.-W.L.; methodology, Y.-W.L.; software, Y.-W.L.; validation, P.-Y.W., T.-Y.L. and T.W.; formal analysis, P.-Y.W., T.-Y.L. and Y.-W.L.; investigation, P.-Y.W.; resources, Y.-W.L.; data curation, P.-Y.W. and T.-Y.L.; writing—original draft preparation, Y.-W.L.; writing—review and editing, T.W. and Y.-W.L.; visualization, Y.-W.L.; supervision, Y.-W.L.; project administration, Y.-W.L.; funding acquisition, Y.-W.L. All authors have read and agreed to the published version of the manuscript.

Funding: This study was supported by the Ministry of Science and Technology of Taiwan under contract (MOST 110-2113-M-018-001).

Conflicts of Interest: The authors declare no conflict of interest.

References

1. Su, Y. Revisiting carbon, nitrogen, and phosphorus metabolisms in microalgae for wastewater treatment. *Sci. Total Environ.* **2021**, *762*, 144590. [CrossRef] [PubMed]
2. Saeed, M.; Khan, I.; Adeel, M.; Akram, N.; Muneer, M. Synthesis of CoO-ZnO photocatalyst for enhanced visible-light assisted photodegradation of methylene blue. *New J. Chem.* **2022**. [CrossRef]
3. Nipa, S.T.; Akter, R.; Raihan, A.; Rasul, S.B.; Som, U.; Ahmed, S.; Alam, J.; Khan, M.R.; Enzo, S.; Rahman, W. State-of-the-art biosynthesis of tin oxide nanoparticles by chemical precipitation method towards photocatalytic application. *Environ. Sci. Pollut. Res.* **2022**. [CrossRef] [PubMed]
4. Varsha, M.; Kumar, P.S.; Rathi, B.S. A review on recent trends in the removal of emerging contaminants from aquatic environment using low-cost adsorbents. *Chemosphere* **2022**, *287*, 132270. [CrossRef]
5. Bilińska, L.; Gmurek, M. Novel trends in AOPs for textile wastewater treatment. Enhanced dye by-products removal by catalytic and synergistic actions. *Water Resour. Ind.* **2021**, *26*, 100160. [CrossRef]
6. Qasem, N.A.; Mohammed, R.H.; Lawal, D.U. Removal of heavy metal ions from wastewater: A comprehensive and critical review. *NPJ Clean Water* **2021**, *4*, 36. [CrossRef]
7. Kamran, U.; Bhatti, H.N.; Noreen, S.; Tahir, M.A.; Park, S.-J. Chemically modified sugarcane bagasse-based biocomposites for efficient removal of acid red 1 dye: Kinetics, isotherms, thermodynamics, and desorption studies. *Chemosphere* **2022**, *291*, 132796. [CrossRef]
8. Kamran, U.; Bhatti, H.N.; Iqbal, M.; Jamil, S.; Zahid, M. Biogenic synthesis, characterization and investigation of photocatalytic and antimicrobial activity of manganese nanoparticles synthesized from Cinnamomum verum bark extract. *J. Mol. Struct.* **2019**, *1179*, 532–539. [CrossRef]
9. Li, J.; He, C.; Cao, X.; Sui, H.; Li, X.; He, L. Low temperature thermal desorption-chemical oxidation hybrid process for the remediation of organic contaminated model soil: A case study. *J. Contam. Hydrol.* **2021**, *243*, 103908. [CrossRef]
10. Huang, R.; Zhu, Y.; Curnan, M.T.; Zhang, Y.; Han, J.W.; Chen, Y.; Huang, S.; Lin, Z. Tuning reaction pathways of peroxymonosulfate-based advanced oxidation process via defect engineering. *Cell Rep. Phys. Sci.* **2021**, *2*, 100550. [CrossRef]
11. Sun, Y.; Li, D.; Zhou, S.; Shah, K.J.; Xiao, X. Research Progress of Advanced Oxidation Water Treatment Technology. *Adv. Waterwater Treat. II* **2021**, *102*, 1–47.
12. Walton, J.; Labine, P.; Reidies, A. The chemistry of permanganate in degradative oxidations. In *Chemical Oxidation*; Eckenfelder, W.W., Bowers, A.R., Roth, J.A., Eds.; Technomic Publishing Co., Inc.: Lancaster, Basel, 1991; Volume 1, pp. 205–219.
13. Luo, H.; Zeng, Y.; He, D.; Pan, X. Application of iron-based materials in heterogeneous advanced oxidation processes for wastewater treatment: A review. *Chem. Eng. J.* **2021**, *407*, 127191. [CrossRef]
14. Sgroi, M.; Anumol, T.; Vagliasindi, F.G.; Snyder, S.A.; Roccaro, P. Comparison of the new Cl_2/O_3/UV process with different ozone-and UV-based AOPs for wastewater treatment at pilot scale: Removal of pharmaceuticals and changes in fluorescing organic matter. *Sci. Total Environ.* **2021**, *765*, 142720. [CrossRef] [PubMed]
15. Deniere, E.; Alagappan, R.P.; Van Langenhove, H.; Van Hulle, S.; Demeestere, K. The ozone-activated peroxymonosulfate process (O_3/PMS) for removal of trace organic contaminants in natural and wastewater: Effect of the (in) organic matrix composition. *Chem. Eng. J.* **2022**, *430*, 133000. [CrossRef]
16. Ganiyu, S.O.; Zhou, M.; Martinez-Huitle, C.A. Heterogeneous electro-Fenton and photoelectro-Fenton processes: A critical review of fundamental principles and application for water/wastewater treatment. *Appl. Catal. B Environ.* **2018**, *235*, 103–129. [CrossRef]
17. Labiadh, L.; Ammar, S.; Kamali, A.R. Oxidation/mineralization of AO7 by electro-Fenton process using chalcopyrite as the heterogeneous source of iron and copper catalysts with enhanced degradation activity and reusability. *J. Electroanal. Chem.* **2019**, *853*, 113532. [CrossRef]
18. Ribeiro, J.P.; Nunes, M.I. Recent trends and developments in Fenton processes for industrial wastewater treatment–A critical review. *Environ. Res.* **2021**, *197*, 110957. [CrossRef]
19. Mahtab, M.S.; Farooqi, I.H.; Khursheed, A. Sustainable approaches to the Fenton process for wastewater treatment: A review. *Mater. Today* **2021**, *47*, 1480–1484. [CrossRef]

20. Liang, S.; Ziyu, Z.; Fulong, W.; Maojuan, B.; Xiaoyan, D.; Lingyun, W. Activation of persulfate by mesoporous silica spheres-doping CuO for bisphenol A removal. *Environ. Res.* **2022**, *205*, 112529. [CrossRef]
21. Liang, S.; Ziyu, Z.; Han, J.; Xiaoyan, D. Facile synthesis of magnetic mesoporous silica spheres for efficient removal of methylene blue via catalytic persulfate activation. *Sep. Purif. Technol.* **2021**, *256*, 117801. [CrossRef]
22. Kiejza, D.; Kotowska, U.; Polińska, W.; Karpińska, J. Peracids-New oxidants in advanced oxidation processes: The Use of peracetic acid, peroxymonosulfate, and persulfate salts in the removal of organic micropollutants of emerging concern—A review. *Sci. Total Environ.* **2021**, *790*, 148195. [CrossRef] [PubMed]
23. Zhang, B.-T.; Wang, Q.; Zhang, Y.; Teng, Y.; Fan, M. Degradation of ibuprofen in the carbon dots/Fe_3O_4@carbon sphere pomegranate-like composites activated persulfate system. *Sep. Purif. Technol.* **2020**, *242*, 116820. [CrossRef]
24. Feng, Y.; Zhong, J.; Zhang, L.; Fan, Y.; Yang, Z.; Shih, K.; Li, H.; Wu, D.; Yan, B. Activation of peroxymonosulfate by Fe^0@Fe_3O_4 core-shell nanowires for sulfate radical generation: Electron transfer and transformation products. *Sep. Purif. Technol.* **2020**, *247*, 116942. [CrossRef]
25. Tan, C.; Xu, Q.; Sheng, T.; Cui, X.; Wu, Z.; Gao, H.; Li, H. Reactive oxygen species generation in FeOCl nanosheets activated peroxymonosulfate system: Radicals and non-radical pathways. *J. Hazard. Mater.* **2020**, *398*, 123084. [CrossRef]
26. Sun, L.; Hu, D.; Zhang, Z.; Deng, X. Oxidative degradation of methylene blue via PDS-based advanced oxidation process using natural pyrite. *Int. J. Environ. Res. Public Health* **2019**, *16*, 4773. [CrossRef]
27. Zhu, Y.; Liu, Y.; Li, P.; Zhang, Y.; Wang, G.; Zhang, Y. A comparative study of peroxydisulfate and peroxymonosulfate activation by a transition metal–H_2O_2 system. *Environ. Sci. Pollut. Res.* **2021**, *28*, 47342–47353. [CrossRef]
28. Ghanbari, F.; Khatebasreh, M.; Mahdavianpour, M.; Mashayekh-Salehi, A.; Aghayani, E.; Lin, K.-Y.A.; Noredinvand, B.K. Evaluation of peroxymonosulfate/O_3/UV process on a real polluted water with landfill leachate: Feasibility and comparative study. *Korean J. Chem. Eng.* **2021**, *38*, 1416–1424. [CrossRef]
29. Dung, N.T.; Thao, V.D.; Huy, N.N. Decomposition of glyphosate in water by peroxymonosulfate activated with CuCoFe-LDH material. *Vietnam J. Chem.* **2021**, *59*, 813–822.
30. Wang, W.; Chen, M.; Wang, D.; Yan, M.; Liu, Z. Different activation methods in sulfate radical-based oxidation for organic pollutants degradation: Catalytic mechanism and toxicity assessment of degradation intermediates. *Sci. Total Environ.* **2021**, *772*, 145522. [CrossRef]
31. Xu, X.; Tang, D.; Cai, J.; Xi, B.; Zhang, Y.; Pi, L.; Mao, X. Heterogeneous activation of peroxymonocarbonate by chalcopyrite ($CuFeS_2$) for efficient degradation of 2, 4-dichlorophenol in simulated groundwater. *Appl. Catal. B Environ.* **2019**, *251*, 273–282. [CrossRef]
32. Karim, A.V.; Jiao, Y.; Zhou, M.; Nidheesh, P. Iron-based persulfate activation process for environmental decontamination in water and soil. *Chemosphere* **2021**, *265*, 129057. [CrossRef] [PubMed]
33. Hou, K.; Pi, Z.; Yao, F.; Wu, B.; He, L.; Li, X.; Wang, D.; Dong, H.; Yang, Q. A critical review on the mechanisms of persulfate activation by iron-based materials: Clarifying some ambiguity and controversies. *Chem. Eng. J.* **2021**, *407*, 127078. [CrossRef]
34. Zheng, X.; Niu, X.; Zhang, D.; Lv, M.; Ye, X.; Ma, J.; Lin, Z.; Fu, M. Metal-based catalysts for persulfate and peroxymonosulfate activation in heterogeneous ways: A review. *Chem. Eng. J.* **2022**, *429*, 132323. [CrossRef]
35. Li, B.; Wang, Y.-F.; Zhang, L.; Xu, H.-Y. Enhancement strategies for efficient activation of persulfate by heterogeneous cobalt-containing catalysts: A review. *Chemosphere* **2021**, *291*, 132954. [CrossRef]
36. Fayyaz, A.; Saravanakumar, K.; Talukdar, K.; Kim, Y.; Yoon, Y.; Park, C.M. Catalytic oxidation of naproxen in cobalt spinel ferrite decorated $Ti_3C_2T_x$ MXene activated persulfate system: Mechanisms and pathways. *Chem. Eng. J.* **2021**, *407*, 127842. [CrossRef]
37. Nie, W.; Mao, Q.; Ding, Y.; Hu, Y.; Tang, H. Highly efficient catalysis of chalcopyrite with surface bonded ferrous species for activation of peroxymonosulfate toward degradation of bisphenol A: A mechanism study. *J. Hazard. Mater.* **2019**, *364*, 59–68. [CrossRef]
38. Huang, X.; Zhu, T.; Duan, W.; Liang, S.; Li, G.; Xiao, W. Comparative studies on catalytic mechanisms for natural chalcopyrite-induced Fenton oxidation: Effect of chalcopyrite type. *J. Hazard. Mater.* **2020**, *381*, 120998. [CrossRef]
39. Li, Y.; Dong, H.; Li, L.; Tang, L.; Tian, R.; Li, R.; Chen, J.; Xie, Q.; Jin, Z.; Xiao, J. Recent advances in wastewater treatment through transition metal sulfides-based advanced oxidation processes. *Water Res.* **2021**, *192*, 116850. [CrossRef]
40. Xia, Q.; Zhang, D.; Yao, Z.; Jiang, Z. Investigation of Cu heteroatoms and Cu clusters in Fe-Cu alloy and their special effect mechanisms on the Fenton-like catalytic activity and reusability. *Appl. Catal. B Environ.* **2021**, *299*, 120662. [CrossRef]
41. Xia, Q.; Zhang, D.; Yao, Z.; Jiang, Z. Revealing the enhancing mechanisms of Fe–Cu bimetallic catalysts for the Fenton-like degradation of phenol. *Chemosphere* **2022**, *289*, 133195. [CrossRef]
42. Da Silveira Salla, J.; da Boit Martinello, K.; Dotto, G.L.; García-Díaz, E.; Javed, H.; Alvarez, P.J.; Foletto, E.L. Synthesis of citrate–modified $CuFeS_2$ catalyst with significant effect on the photo–Fenton degradation efficiency of bisphenol a under visible light and near–neutral pH. *Colloid Surf. A Physicochem. Eng. Asp.* **2020**, *595*, 124679. [CrossRef]
43. Ltaïef, A.H.; Pastrana-Martínez, L.M.; Ammar, S.; Gadri, A.; Faria, J.L.; Silva, A.M. Mined pyrite and chalcopyrite as catalysts for spontaneous acidic pH adjustment in Fenton and LED photo-Fenton-like processes. *J. Chem. Technol. Biotechnol.* **2018**, *93*, 1137–1146. [CrossRef]
44. Chang, S.-A.; Wen, P.-Y.; Wu, T.; Lin, Y.-W. Microwave-Assisted Synthesis of Chalcopyrite/Silver Phosphate Composites with Enhanced Degradation of Rhodamine B under Photo-Fenton Process. *Nanomaterials* **2020**, *10*, 2300. [CrossRef] [PubMed]

45. Kamran, U.; Park, S.-J. Hybrid biochar supported transition metal doped MnO_2 composites: Efficient contenders for lithium adsorption and recovery from aqueous solutions. *Desalination* **2022**, *522*, 115387. [CrossRef]
46. Kamran, U.; Park, S.-J. Acetic acid-mediated cellulose-based carbons: Influence of activation conditions on textural features and carbon dioxide uptakes. *J. Colloid Interface Sci.* **2021**, *594*, 745–758. [CrossRef] [PubMed]
47. Kamran, U.; Park, S.-J. Tuning ratios of KOH and NaOH on acetic acid-mediated chitosan-based porous carbons for improving their textural features and CO_2 uptakes. *J. CO2 Util.* **2020**, *40*, 101212. [CrossRef]
48. Ghahremaninezhad, A.; Dixon, D.; Asselin, E. Electrochemical and XPS analysis of chalcopyrite ($CuFeS_2$) dissolution in sulfuric acid solution. *Electrochim. Acta* **2013**, *87*, 97–112. [CrossRef]
49. Jiang, L.; Luo, Z.; Li, Y.; Wang, W.; Li, J.; Li, J.; Ao, Y.; He, J.; Sharma, V.K.; Wang, J. Morphology-and phase-controlled synthesis of visible-light-activated S-doped TiO_2 with tunable S^{4+}/S^{6+} ratio. *Chem. Eng. J.* **2020**, *402*, 125549. [CrossRef]
50. Liang, C.; Huang, C.-F.; Mohanty, N.; Kurakalva, R.M. A rapid spectrophotometric determination of persulfate anion in ISCO. *Chemosphere* **2008**, *73*, 1540–1543. [CrossRef]
51. Jia, J.; Liu, D.; Wang, S.; Li, H.; Ni, J.; Li, X.; Tian, J.; Wang, Q. Visible-light-induced activation of peroxymonosulfate by TiO_2 nano-tubes arrays for enhanced degradation of bisphenol A. *Sep. Purif. Technol.* **2020**, *253*, 117510. [CrossRef]